ACS APPLIED MATERIALS & INTERFACES

Research Article

www.acsami.org

# Direct Patterning of Conductive Polymer Domains for Photovoltaic Devices

Suchanun Moungthai,[†,§] Nikhila Mahadevapuram,[†,§] Paul Ruchhoeft,[‡] and Gila E. Stein*,[†]

[†]Department of Chemical and Biomolecular Engineering, University of Houston, Houston, Texas 77204-4004, United States

[‡]Department of Electrical and Computer Engineering, University of Houston, Houston, Texas 77204-4004, United States

Supporting Information

**ABSTRACT:** We report a simple approach to control the morphology of polymer/fullerene solar cells based on electron-beam patterning of polymer semiconductors. This process generates conductive nanostructures or microstructures through an in situ cross-linking reaction, where the size, shape, and density of polymer domains are all tunable parameters. Cross-linked polymer structures are resistant to heat and solvents, so they can be incorporated into devices that require thermal annealing or solution-based processing. We demonstrate this method by building "gradient" and nanostructured poly(3-hexylthiophene)/fullerene solar cells. The power-conversion efficiency of these model devices improves with increasing interfacial area. The flexible methodology can be used to study the effects of active layer design on optoelectronic function.

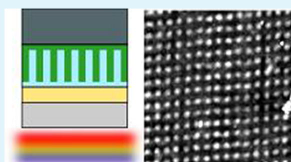

**KEYWORDS:** *organic electronic, P3HT, electron beam lithography, solar cell, photovoltaic, PCBM*

## INTRODUCTION

Polymer solar cells are attractive for clean energy production, because they can be fabricated in lightweight, flexible, durable, and inexpensive modules. The most-efficient devices are based on the bulk heterojunction (BHJ) design.[1,2] BHJs are prepared by arresting the phase separation of a polymer−fullerene (donor−acceptor) blend. The resulting structure is a nanoscale, interpenetrating network that offers a large interfacial area for charge generation and a good pathway for charge transport to the electrodes. Currently, it is unclear what aspects of the BHJ structure are controlling device function, because it is difficult to control and characterize the formation of these highly nonequilibrium morphologies. BHJs are usually prepared by spin-casting from volatile solvents, and the as-cast structure is very sensitive to the solvent quality, evaporation rate, solution concentration, and ambient temperature. BHJ growth kinetics are controlled by a coupled crystallization-diffusion mechanism, so key parameters such as domain size, phase purity, polymer crystallinity, and interfacial area cannot be varied independently. In addition, the BHJ morphology is disordered and anisotropic at both the molecular and nanometer length scales, and this feature complicates measurement of the structure with scattering or microscopy.[3] As a result of these challenges, there is wide debate about the optimal design attributes for polymer-based solar cells. It is generally agreed that charge generation is optimized when the phase separation length scale is comparable to the exciton diffusion length, which is ∼10 nm for most polymer semiconductors. However, even when the average BHJ domain size meets this criteria, the film contains defects such as regions of complete polymer/fullerene miscibility, domains that are larger than the exciton diffusion length, and incomplete paths to the electrodes.[3] These defects are responsible for carrier losses through trapping, recombination, or photoluminescence, making it difficult to interpret spectroscopic and optoelectronic measurements accurately. Furthermore, while most works indicate that highly crystalline polymers will enhance light absorption and carrier transport, there are examples of good optoelectronic function in low-crystallinity systems.[4,5] This discrepancy is explained by the coupling between crystallinity, domain size, and interfacial area in a BHJ device, making it difficult to determine which parameter is controlling the observed photocurrent. It is critical to develop model systems where different structural parameters can be independently interrogated.

A variety of experimental methods have been developed that offer control over the nanoscale morphology.[6] Examples include self-assembly of block copolymer semiconductors,[7−9] polymer nanowire growth,[10−12] and imprint lithography.[13−20] Block copolymers provide a simple route to generate dense arrays of nanostructures, but it is difficult to control domain orientations throughout the film thickness. Furthermore, critical properties such as domain size, interfacial width, and crystallinity are all coupled to the copolymer composition and molecular weight.[21] The growth of crystalline polymer nanowires will produce high-mobility nanoscale domains,[10−12,22] but does not afford precise control over wire diameters, orientations, or placement. Recently, several groups have used imprint lithography to build polymer-based heterojunctions with well-defined morphologies.[6,13−15,18−20,23] Such top-down lithographic techniques provide control over domain sizes and interfacial area, which is helpful to understand the effects of active layer structure on optoelectronic function. For example, these studies have demonstrated that matching the domain size to exciton diffusion lengths can enhance

Received: May 11, 2012
Accepted: July 20, 2012
Published: July 20, 2012

 © 2012 American Chemical Society 

photocurrent generation.[19,20] However, imprint lithography has a few limitations. First, master stamp fabrication is difficult and expensive, particularly when the desired pattern is a large-area array of sub-20-nm nanostructures. Imprint lithography is an excellent strategy for repetitive printing of a single design, but this approach can be costly and time-consuming when many different designs are under investigation. Second, the thermal and mechanical properties of organic semiconductors are not optimized for imprinting. This means that imprinted nanostructures have limited stability through solvent processing or heat treatments, and it is difficult to generate nanostructures with high aspect ratios (width:height > 2).[20] Finally, imprinting will induce alignment of the polymer chains within the template,[15] so polymer crystallinity and grain orientations will be coupled to the design of the stamp.

In this work, we report a flexible approach to control the morphology of polymer/fullerene heterojunctions. Thin films of $\pi$-conjugated polymers are directly patterned with electron-beam lithography (EBL).[24−26] This process initiates a localized, in situ cross-linking reaction that generates conductive nanostructures or microstructures. The image is developed by immersion in an organic solvent, and then the cross-linked polymer structures are coated with a soluble fullerene to complete the heterojunction. This protocol allows for independent variation of domain size and shape, interfacial area, and phase purity. The lithographic process is compatible with commercially available materials such as different types of poly(3-alkylthiophene) and poly(phenylene vinylene).[24−26] Polymer cross-link density can be tuned *on-demand* by varying the exposure dose, providing a simple route to engineer high-performance nanostructures that are stable through solvent and thermal processing. Furthermore, after evaluating the spectroscopic and optoelectronic properties of these devices, the heterojunction morphology can be measured with microscopy by "deconstructing" the active layer. While EBL is too slow for manufacturing, this technology is very valuable for structure−property investigations: EBL patterns are defined with computer-aided design ("maskless"), so different types of designs can be rapidly evaluated. State-of-the-art EBL systems require a substantial capital investment, but the data presented in this report were acquired with a scanning electron microscopy (SEM) system that was equipped with a Nanometer Pattern Generation System.[27]

The materials used in this work are poly(3-hexylthiophene) (P3HT) and [6,6]-phenyl-$C_{61}$-butyric acid methyl ester (PCBM), which are benchmark donor and acceptor chemistries, respectively.[1,3] This report is divided into three parts. First, we investigated the lithographic properties of P3HT films. We find that P3HT is a high-resolution, negative-tone resist. Second, we measured irradiated P3HT films with ultraviolet−visible (UV−vis) and infrared (IR) absorbance spectroscopies. These data confirm that patterned P3HT films retain the $\pi$-bonds responsible for light absorption, charge generation, and charge transport. Third, we evaluated the electronic performance of patterned P3HT films in "gradient" and nanostructured P3HT/PCBM heterojunctions (see Figure 1). The power-conversion efficiency of lithographically defined heterojunctions improves with increasing polymer/fullerene interfacial area. These results establish a model system for structure−function studies of polymer-based solar cells, where domain size and interfacial area can be varied independent of polymer crystallinity.

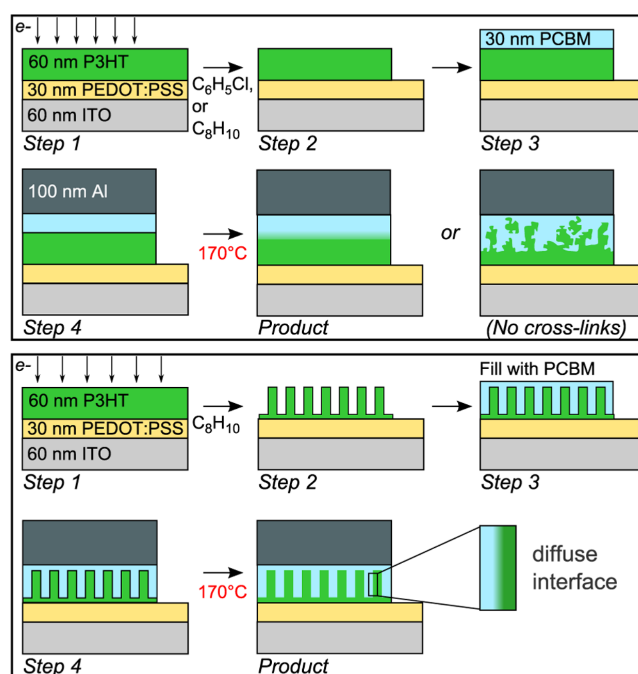


**Figure 1.** Direct patterning of gradient (top) and nanostructured (bottom) polymer/fullerene solar cells. ITO = indium tin oxide; PEDOT:PSS = poly(3,4-ethylenedioxythiophene):poly(styrenesulfonate); P3HT = poly(3-hexylthiophene), PCBM = [6,6]-phenyl-$C_{61}$-butyric acid methyl ester. PCBM is spin-cast from dichloromethane (DCM).

## RESULTS AND DISCUSSION

**Lithography.** Our first aim was to evaluate the sensitivity of P3HT to electron-beam radiation. Thin films of P3HT were patterned with EBL and the relief images were developed with chlorobenzene (room temperature) or *p*-xylene (35 °C). Note that *p*-xylene is purged with nitrogen to displace dissolved oxygen. Figures 2a and 2b include examples of microscale and nanoscale P3HT patterns, respectively, and Figure 2c reports the normalized residual thickness as a function of exposure dose for each developer. We find that P3HT is a high-resolution, negative-tone electron-beam resist. The critical exposure dose at 30 keV is ~400 $\mu C/cm^2$, which is slightly lower than poly(methyl methacrylate) (PMMA) or hydrogen silsesquioxane electron-beam resists.[28,29] It is difficult to evaluate the resolution limit for P3HT, because our EBL system does not have instrumentation for dynamic focus corrections. However, we find that nanodots and nanolines with 50-nm widths are reliably resolved using a low beam current, and we anticipate that even smaller features can be printed with a more-sophisticated EBL system and/or an optimized development protocol.[28,30] We also evaluated the sensitivity of poly(3,4-ethylenedioxythiophene):poly(styrenesulfonate) (PEDOT:PSS) to electron-beam radiation. This material is used as a hole-injection layer at the anode (see Figure 1) and is therefore irradiated during the fabrication process. We find that PEDOT:PSS is also a negative-tone material, but with a low critical exposure dose of 200 $\mu C/cm^2$ for development in water (see the Supporting Information). It is important to note that critical exposure doses are very sensitive to polymer molecular weight. For example, increasing the molecular weight of P3HT will reduce the required dose.

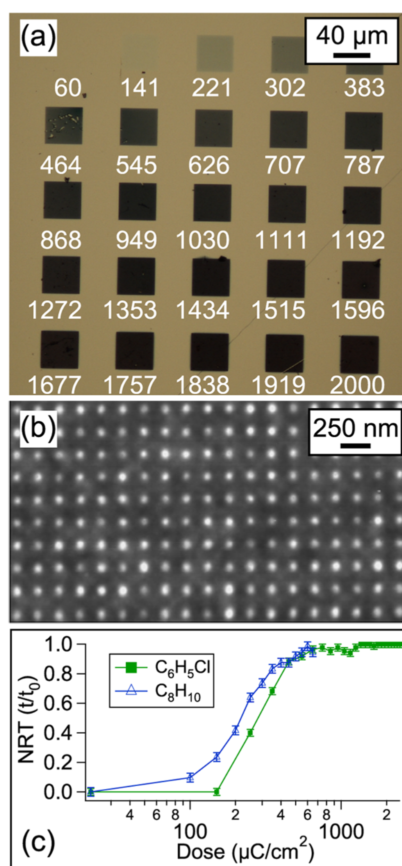


**Figure 2.** (a) Optical micrograph of cross-linked P3HT pads on a silicon substrate. Irradiation doses are marked below each pad in units of $\mu$C/cm$^2$. (b) Example of P3HT nanopillar arrays patterned with an area dose of 450 $\mu$C/cm$^2$. Average pillar diameter and height are 50 and 60 nm, respectively. Image was acquired with an atomic force microscope operating in tapping-mode. (c) Normalized residual thickness ($t/t_0$) as a function of exposure dose for chlorobenzene (square) and *p*-xylene (triangle) developers.

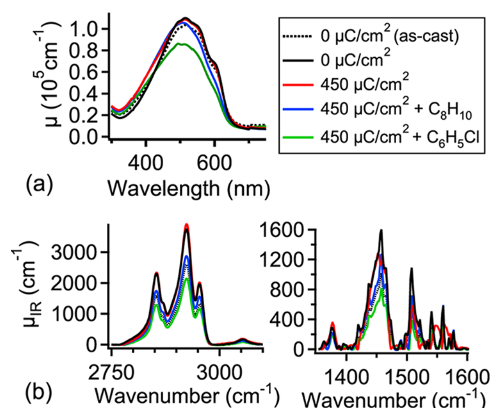


**Figure 3.** (a) Linear absorption coefficient ($\mu$) measured by UV–vis and (b) IR absorbance spectra of P3HT films at different stages in the lithographic process.

**Spectroscopy.** Our second aim was to determine if irradiated P3HT films retain the $\pi$-bonds responsible for optoelectronic function. There are several studies that have considered P3HT as a resist for optical lithography, where irradiation in air will initiate complex photo-oxidation reactions that result in cross-linking and loss of conjugation.[24,31−33] Our studies differ because EBL is implemented under ultrahigh vacuum ($10^{-7}$ Torr). The irradiated sample volume is very small, and this prevents detailed characterization of the bond structure with nuclear magnetic resonance (NMR spectroscopy) or X-ray photoelectron spectroscopy (XPS). Instead, we used UV–vis and IR absorbance spectroscopies to evaluate the properties of unexposed films, irradiated films, and irradiated films after immersion in developer. Representative UV–vis and IR absorbance data are included in Figure 3 for five samples: an as-cast P3HT film, a "pre-baked" P3HT film that was thermally annealed for 2 min at 150 °C, a prebaked P3HT film that was irradiated at 450 $\mu$C/cm$^2$, and prebaked P3HT films that were irradiated at 450 $\mu$C/cm$^2$ and then immersed in chlorobenzene or *p*-xylene. These data are normalized to account for variations in film thickness. First, the linear absorption coefficients ($\mu$) for as-prepared and irradiated P3HT films are nearly identical. This finding is consistent with work from Gearba et al., where thin P3HT films were thermally cross-linked with a peroxide radical initiator, and there was no change in UV–vis absorbance at low-to-moderate cross-link densities.[34] However, we do find evidence of photobleaching when irradiated films are immersed in the developer. The wavelength at peak absorbance is (515 ± 2) nm, (513 ± 2) nm, and (509 ± 2) nm for as-prepared, irradiated, and developed films, respectively. [Note that average values and standard deviations are calculated from measurements of 5–10 samples at each step in the process.] In addition to this blue-shift, developed films absorb less light and exhibit weaker vibronic shoulders.[35,36] The loss of fine structure suggests that development partly disrupts the intermolecular ordering, and this conclusion is supported by preliminary grazing-incidence wide-angle X-ray scattering (GIWAXS) data that are included in the Supporting Information. Second, the IR spectra for as-prepared and irradiated films are nearly identical. Peaks associated with hydrocarbon and aromatic functional groups are resolved in the ranges of 2850–3050 cm$^{-1}$ and 1370–1560 cm$^{-1}$, respectively, although the latter fingerprint region is quite noisy. All peak intensities are weaker after development, which is expected based on the reduced film thickness, but this finding is also consistent with polymer degradation.[33,37]

It is difficult to identify the P3HT cross-linking reaction using UV–vis and IR absorbance data. We have hypothesized a mechanism in the Supporting Information that is consistent with other studies.[26,37] For the purposes of this discussion, it is important to note that electron beams will ionize the polymer to generate radicals. The data reported in Figure 2 demonstrate that some of these radicals combine to form intermolecular cross-links. P3HT is a semicrystalline polymer with a glass-transition temperature near 12 °C,[38] although this value is widely debated,[39,40] so cross-links are most likely formed in the amorphous regions where the polymer has greater segmental mobility. There is a high probability that some radicals remain trapped in the polymer, and a subsequent reaction during development could explain the changes in UV–vis and IR absorbance that are summarized in Figure 3. Indirect evidence of trapped radicals is included in the Supporting Information, where we show that a post-exposure bake at elevated temperature increases the size of the nanostructures; in other words, baking enhances the polymer mobility so more radicals can meet and react. One possibility is that trapped radicals can react with dissolved oxygen in the solvent. The IR measurements do not detect any oxidation products such as carbonyl and hydroxyl moieties, but the UV–vis spectra suggest that

Table 1. Electronic Performance of P3HT/PCBM Solar Cells after 4 min of Annealing at 170 °C, Unless Otherwise Noted

| design[a] | dose ($\mu$C/cm$^2$) | developer | $V_{oc}$ (V) | $J_{sc}$ (mA/cm$^2$) | FF | PCE (%) |
|---|---|---|---|---|---|---|
| BHJ | 0 | N/A | 0.60 ± 0.01 | 8.86 ± 3.01 | 0.46 ± 0.06 | 2.45 ± 0.85 |
| SC | 0 | N/A | 0.56 ± 0.04 | 7.59 ± 2.48 | 0.43 ± 0.03 | 1.85 ± 0.73 |
| Gr | 300 | $C_6H_5Cl$ | 0.56 ± 0.01 | 2.67 ± 1.32 | 0.36 ± 0.03 | 0.55 ± 0.33 |
| Gr | 450 | $C_6H_5Cl$ | 0.57 ± 0.04 | 3.07 ± 1.25 | 0.35 ± 0.01 | 0.61 ± 0.27 |
| Gr | 600 | $C_6H_5Cl$ | 0.58 ± 0.02 | 1.51 ± 0.66 | 0.34 ± 0.01 | 0.30 ± 0.15 |
| Gr | 300 | $C_8H_{10}$ | 0.58 ± 0.03 | 1.47 ± 0.32 | 0.34 ± 0.01 | 0.29 ± 0.08 |
| Gr | 450 | $C_8H_{10}$ | 0.59 ± 0.02 | 1.24 ± 0.30 | 0.36 ± 0.03 | 0.33 ± 0.10 |
| Gr | 600 | $C_8H_{10}$ | 0.60 ± 0.02 | 1.38 ± 0.02 | 0.35 ± 0.02 | 0.29 ± 0.01 |
| NP[c] | 450 | $C_8H_{10}$ | 0.60 ± 0.01 | 1.79 ± 0.16 | 0.40 ± 0.03 | 0.43 ± 0.02 |
| MNL[b,c] | 450 | $C_8H_{10}$ | 0.61 | 1.78 | 0.47 | 0.51 |

[a]BHJ = bulk heterojunction, SC = sequential casting, Gr = gradient, NP = square grid of nanopillars with 400-nm pitch, MNL = modulated nanolines with a 400-nm pitch. [b]Only one device was prepared in this manner, so we do not report the uncertainty. [c]Data are reported for 1 min of annealing at 170 °C.

purified *p*-xylene can minimize photobleaching, compared with out-of-the-bottle chlorobenzene. Another possibility is that residual iron catalyst from the polymer synthesis is sensitized by electron-beam radiation, generating free radicals that could attack the thienyl ring and reduce the extent of conjugation.[37] This explanation is consistent with UV−vis and IR absorbance spectra. Further investigations are underway to identify the photobleaching mechanism and address this challenge.

With regards to PEDOT:PSS, irradiation slightly increases the UV−vis absorbance at 437 nm, while no clear changes are detected in IR absorbance spectra (see the Supporting Information). Other works suggest that low-energy electrons (ca. 3 eV) can induce oxygen and sulfur loss from PSS and disrupt carbon−oxygen bonds in PEDOT,[41] while the thiophene rings are unaffected by irradiation. We find that irradiated PEDOT:PSS films are insoluble in water, which is consistent with a reduction of PSS solubility due to sulfonate damage and/or intermolecular cross-linking through ionization of the polymers.

**Optoelectronic Function.** Our final aim was to characterize the electronic performance of lithographically patterned P3HT films in P3HT/PCBM solar cells. We built "gradient" and nanostructured P3HT/PCBM heterojunctions following the schemes in Figure 1. The variables in these experiments were exposure dose and type of developer: Patterns were defined with an area dose of 300, 450, or 600 $\mu$C/cm$^2$, and then developed with either chlorobenzene or *p*-xylene. We also prepared two types of samples that were not exposed to electron-beam radiation: BHJs based on P3HT/PCBM blends, and devices that were prepared by sequential casting of P3HT and PCBM layers from orthogonal solvents.[42−44] Table 1 summarizes the average photovoltaic response for all devices after annealing for 1−4 min at 170 °C. Before discussing the lithographically defined heterojunctions, we note that the electronic characteristics of BHJ and sequentially cast samples are very similar. This finding indicates that sequential casting generates a bicontinuous morphology during thermal annealing,[43−45] which is expected based on the well-documented miscibility of P3HT and PCBM and fast interdiffusion rates.[46−48] We also note two significant differences between our work and others in the literature. First, the device active areas are small (ca. 0.03−0.05 cm$^2$), so edge effects could inflate the measured short-circuit current density.[49,50] Second, the cathode is Al rather than the optimal LiF/Al design, and this leads to inferior power-conversion efficiency.[51,52] With these factors in mind, the device characteristics in this report should be compared against each other rather than other works.

The power-conversion efficiencies (PCEs) of lithographically defined gradient devices range from 0.3% to 0.6%, while the PCE of BHJ and sequentially cast samples is ∼2%. This difference stems from smaller fill factors (FF) and short-circuit current densities ($J_{sc}$) when the active layer is built with EBL. The open-circuit voltage ($V_{oc}$) is not affected by the lithographic process. There are two likely causes for diminished electronic performance of electron-beam patterned heterojunctions. First, the lithographic process may change the P3HT chemistry. The data included in Figure 3 demonstrate that patterned P3HT films are adversely affected by development and absorb less light. Irradiation could have other consequences that are not yet understood, such as introduction of trap states that reduce the carrier mobility. Second, cross-linking the P3HT film will prevent the formation of a nanoscale P3HT/PCBM network during thermal annealing. The smaller interfacial area in gradient devices will reduce the density of photogenerated charges. We note that other studies of planar P3HT/PCBM heterojunctions report similar values for PCE (ca. 0.5%) in the absence of P3HT-PCBM interdiffusion,[20,45] although it is difficult to compare these data against ours, because of the differences in device layout and processing methods.

The spectroscopy data in Figure 3 suggest that purified *p*-xylene is more effective at suppressing photobleaching than chlorobenzene. However, as summarized in Table 1, development with chlorobenzene can yield higher values of PCE than *p*-xylene. This finding might suggest that chlorobenzene is the better developer, but there are two observations that lead us to select *p*-xylene instead. First, there is less sample-to-sample variability when developing with *p*-xylene, compared with chlorobenzene. These statistics are included in Table 1. Second, development with *p*-xylene yields heterojunctions with better thermal stability than chlorobenzene. Figure 4 reports the current density−voltage ($J$−$V$) characteristics of sequentially

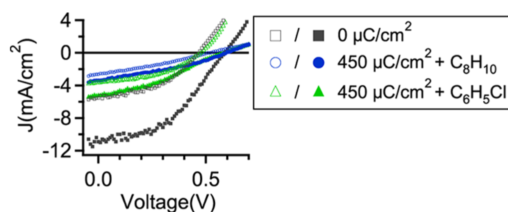


**Figure 4.** *J*−*V* characteristics of sequentially cast (0 μC/cm$^2$) and gradient P3HT/PCBM solar cells. The curves were measured under AM1.5G white-light illumination at 100 mW/cm$^2$. Open/closed symbols correspond with no annealing and 4 min of thermal annealing at 170 °C, respectively.

cast and gradient devices, both before and after thermal annealing for 4 min at 170 °C. Figure 5 reports the power-

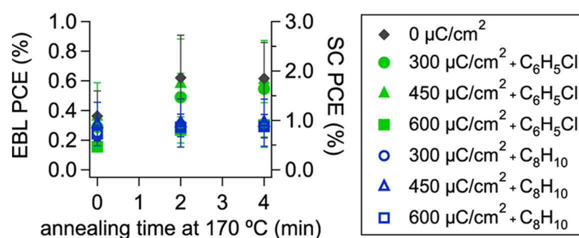


**Figure 5.** Power-conversion efficiency (PCE) of sequentially cast (SC) and gradient (EBL) P3HT/PCBM devices as a function of annealing time. The PCE of sequentially cast devices is denoted by 0 μC/cm$^2$ (diamonds), and PCE of lithographically defined gradient devices is reported as a function of dose and type of developer (circles, triangles, and squares).

conversion efficiency as a function of annealing time for all gradient devices. The same trends are observed for sequentially cast devices and gradient heterojunctions that were developed with chlorobenzene: After annealing, the PCE is doubled due to improvements in $V_{oc}$, FF, and $J_{sc}$. In contrast, gradient heterojunctions that were developed with *p*-xylene are nearly unchanged by subsequent thermal annealing (∼10% improvement in PCE).

The average electronic characteristics of lithographically defined gradient heterojunctions are independent of exposure dose, although sample-to-sample variability is minimized by increasing the exposure dose. Such improvements in reproducibility are explained by the lithographic contrast curve in Figure 2. The slope of the contrast curve is a maximum when the exposure dose is 200−400 μC/cm$^2$, which means that a slight variation in beam current or development time will change the residual thickness of the P3HT film. The contrast curve is flat when the dose exceeds 500 μC/cm$^2$, so the process is less sensitive to human error above this threshold. Other studies have demonstrated that PCE in gradient P3HT/PCBM heterojunctions is very sensitive to the thickness of P3HT films, and variations at the scale of 10 nm can change $J_{sc}$ by a factor of 2.[53] This sensitivity to film thickness might explain why $J_{sc}$ seems to vary with the type of developer, because the residual film thickness will differ for chlorobenzene and *p*-xylene.

We used electron-beam patterning to build nanostructured heterojunctions based on arrays of P3HT nanopillars. The diameter and height of these P3HT pillars are ∼220 and 35 nm, respectively, and the pitch is 400 nm. The patterns were exposed with an area dose of 450 μC/cm$^2$ and then developed with *p*-xylene. This process leaves ∼40 nm of cross-linked P3HT underneath the pillars, a consequence of electron scattering events, so the anode is coated with a continuous P3HT film (see Figure 1). The P3HT nanostructures are then spin-coated with PCBM. We found that PCBM tends to dewet from the top edges of the pillars, and measurements of this phenomena are included in Figures 6a−c. This problematic behavior is mitigated by "double-coating" PCBM, which fills the voids and generates a topcoat that is 20−40 nm thick for most devices (described in the Experimental Section). We evaluated the internal structure of these "double-coated" heterojunctions with successive etching and imaging steps, and we determined that PCBM infiltrates the void space and contacts the P3HT

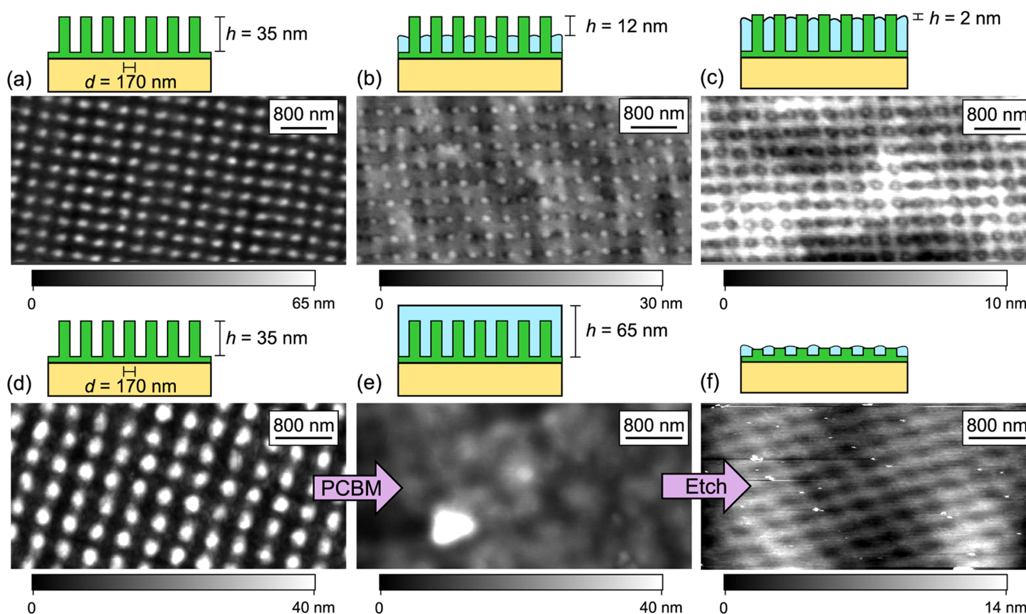


**Figure 6.** Filling P3HT nanopillars with PCBM: (a) initial P3HT nanopillar array; (b) partially filled pillars; and (c) almost complete filling. Note that PCBM slightly dewets from the top edges of the pillars and accumulates in the center of the void space. Internal device structure: (d) initial P3HT nanopillar array; (e) nanopillars after double-coat with PCBM and thermal anneal; and (f) etched to the bottom of the pillars.

pillars throughout the active layer thickness. These data are reported in Figures 6d−f.

The average PCE for nanopillar devices is ~30% larger than the gradient heterojunctions, because of enhancements in $J_{sc}$ and FF. While the lithographic process may change the chemistry of P3HT, these effects are similar for gradient and nanostructured devices. Therefore, we attribute the improved performance of nanopillar devices to the ca. 15% increase in polymer/fullerene interfacial area. Tuning the nanopillar dimensions could further improve the PCE: Currently, the nanopillar diameter is much larger than the exciton diffusion length,[54] and the nanopillar height is smaller than the P3HT absorption length.

Uniquely, after measuring the $J-V$ characteristics of nanostructured devices, we deconstructed the active layer to image the morphology. Deconstruction is a simple, two-step process: The Al cathode is removed with a drop of aqueous potassium hydroxide (KOH) solution, and then the PCBM phase is washed away with dichloromethane (DCM). Figure 7

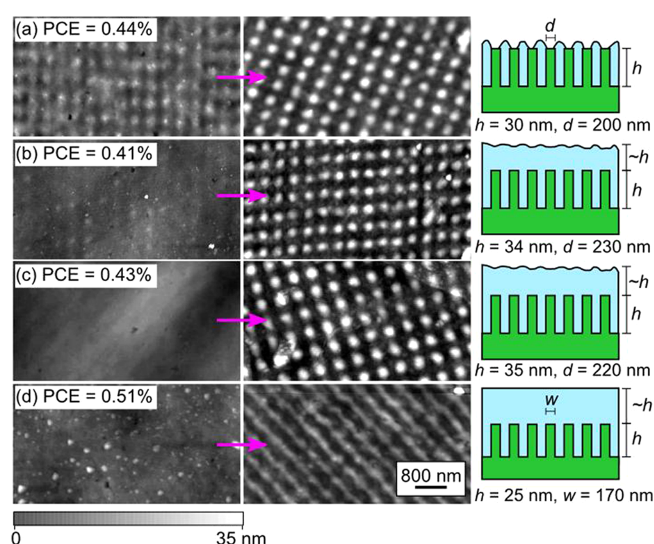


**Figure 7.** Device deconstruction. Surface of the nanostructured P3HT/PCBM composite after removal of Al cathode (left), and after immersion in dichloromethane (right). The accompanying cartoons on the far right side illustrate the active layer structure.

reports atomic force microscopy (AFM) measurements for each step of the deconstruction process, and the accompanying cartoons illustrate the device structure. The deconstruction process facilitates the correlation of active layer morphology and optoelectronic performance. For example, we found one device where an error in the printing process generated "modulated" nanolines instead of dots, and the PCE for this design was 50% larger than gradient devices (see Table 1). Significantly, the P3HT nanostructures are still intact after thermal annealing, solvent-based processing, and electronic characterization steps. Additional stability data are provided in the Supporting Information. We note that polymer-based electronics have limited resistance to thermal or solution-based processing, and this challenge is usually addressed by synthesizing polymer semiconductors with cross-linkable side groups.[53,55−58] In our approach, polymer cross-linking is inherent to the lithographic process. Cross-link density is controlled by exposure dose, so properties such as thermal stability, mechanical stability, and solvent resistance are easy to optimize for a specific application.

## ■ CONCLUSIONS

We developed a simple, two-stage approach to control the morphology of polymer/fullerene solar cells based on direct-write lithography of polymer semiconductors. First, thin films of poly(3-hexylthiophene) (P3HT) are cross-linked into conductive nanostructures or microstructures with electron-beam lithography (EBL). Second, the polymer structures are coated with a soluble fullerene to complete the heterojunction. This methodology offers several features that are very valuable for fundamental structure−property investigations. First, the lithographic process is compatible with commercially available materials. Second, the cross-linked polymer structures are stable through thermal annealing and solution-based processing. Third, different designs can be studied systematically because nanostructure size, shape, density, and placement are all controlled with computer software. Fourth, interfacial area and domain size can be varied independent of polymer crystallinity. Finally, after measuring the optoelectronic characteristics of these model devices, the active layer can be deconstructed to measure the morphology. We verified that patterned P3HT films can absorb light, generate charges, and conduct charges. We included simple structure−property studies that show improvements in power-conversion efficiency with increasing P3HT/fullerene interfacial area. Further studies are needed to fully evaluate the effects of irradiation and development on molecular structure, crystallinity, and charge-carrier mobility.

EBL is too slow for the large-scale production of polymer-based optoelectronic devices. However, like electrochemical nanopatterning and other scanning-probe techniques,[59−62] direct-write lithography could be very valuable for basic scientific investigations. For example, when nanoscale polymer devices are generated in situ with lithography, their positions are precisely controlled for integration into circuity. This attribute is very useful for testing the function of nanoscale optical and electrical sensors.[58,63,64] The cross-linking reaction is advantageous for devices that require sequential casting of different layers, such as multicolor light-emitting diodes (LEDs)[55] or tandem solar cells.[56] Other lithographic tools based on ionizing radiation may be appropriate for manufacturing. For example, ion beams effect the same cross-linking reaction as electrons—but at much lower doses (see Supporting Information). Proximity ion beam lithography systems can provide high throughput (on the order of square meters per hour),[65−68] offering a route to low-cost nano-patterning of polymer semiconductors for a variety of applications.

## ■ EXPERIMENTAL SECTION

**Active Materials.** Poly(3,4-ethylenedioxythiophene):poly-(styrenesulfonate) (PEDOT:PSS) was purchased from Baytron (Product PH500, 1 wt % aqueous dispersion). The PEDOT:PSS dispersion was diluted with two parts deionized water and then filtered using a 0.45-$\mu$m glass microfiber mesh. Poly(3-hexylthiophene) (P3HT) was purchased from Rieke Metals (90%−94% regioregular, number-average molecular weight of 30 kg/mol, polydispersity index of 1.8). P3HT was dissolved in anhydrous chlorobenzene at a concentration of 0.014 g/mL and filtered three times using a 0.2 $\mu$m Teflon mesh. [6,6]-Phenyl-$C_{61}$-butyric acid methyl ester (PCBM) was purchased from Nano-C. PCBM was suspended in anhydrous dichloromethane (DCM) at concentrations of 0.005 or 0.015 g/mL


dx.doi.org/10.1021/am3008328 | ACS Appl. Mater. Interfaces 2012, 4, 4015−4023

and filtered three times with a 0.2 μm Teflon mesh. Note that high PCBM concentrations are needed to fill nanostructured devices, while low PCBM concentrations are used for gradient or sequential casting designs.

**Electron-Beam Lithography.** Microscale P3HT/PEDOT:PSS pads (45 μm × 45 μm) are patterned with a 30-keV, 12-nA electron beam using a FEI XL-30FEG field-emission scanning electron microscopy (SEM) system that was equipped with a 5 MHz Nanometer Pattern Generation System.[27] Exposures are implemented with a square grid based on a pixel size of 30 nm. Doses are varied in the range of 100−2000 μC/cm$^2$. These microstructures are used for two tasks: (i) Lithographic contrast is evaluated by measuring the residual thickness of isolated pads; and (ii) gradient heterojunctions are built by stitching together arrays of pads to span a total area of 2 mm × 2 mm. This report also includes data for P3HT nanopillars. For the example in Figure 2, the nanopillars are printed in a square grid (250 nm pitch) with a focused 50-pA beam. Patterning with this low beam current demonstrates that P3HT is a high-resolution resist. To fabricate devices, the nanopillars are printed in a single pass with a 400-nm pitch. These exposures use a 12-nA beam (fast) to build nanostructured heterojunctions that span an area of 3 mm × 2 mm. The Supporting Information includes data for nanolines, which are printed with a 12-nA beam, single-pass exposure, 400-nm pitch, and 30-nm pixel size along the line axis. A detailed discussion of EBL exposure schemes is included elsewhere.[69] Note that SEM-based lithography does not have dynamic focus corrections, so P3HT films are nanopatterned with a slightly defocused beam, to minimize variations in feature size.

**P3HT Pattern Development.** P3HT patterns are developed in a nitrogen-purged glovebox following one of two procedures: (1) immersion in chlorobenzene for 25 s at room temperature, using a standard Pyrex beaker; or (2) immersion in *p*-xylenes for 25 s at 35 °C, using a Teflon beaker with nitrogen bubbler. Note that samples are usually developed 12−24 h after patterning. It is possible that the post-exposure delay will impact the lithographic resolution and/or optoelectronic properties of P3HT.

**Microscopy.** The structure of patterned P3HT films is measured with atomic force microscopy (AFM) using a MultiMode 3 system (Veeco) in tapping mode. AFM probes are silicon with a spring constant of 40 N/m, and these tips are most effective when functionalized with hexamethyldisiloxane (to minimize adhesive interactions with the polymer). The structures of microscale and millimeter-scale features are evaluated with a Nikon Eclipse LV100 optical microscope (bright-field optics).

**Spectroscopy.** Irradiated P3HT and PEDOT:PSS films are characterized with ultraviolet−visible (UV−vis) and infrared (IR) absorbance spectroscopies. Samples are prepared by spin-casting thin films on 100-nm-thick silicon nitride ($Si_3N_4$) membranes. P3HT and PEDOT:PSS film thicknesses are ~60 and 30 nm, respectively. All data are collected in transmission mode at normal incidence (approximately). UV−vis absorbance is recorded with a Shimadzu Model UV-2401PC spectrophotometer (200−800 nm), and infrared absorbance is measured with a Nicolet Model 6700 spectrometer. The signal from a clean $Si_3N_4$ membrane was also measured and subtracted from the spectra shown in Figure 3. Note that 5−10 samples were measured at each stage in the lithographic process.

**Gradient Heterojunctions.** Substrates are glass microscope slides coated with 60−100 nm of indium tin oxide (ITO, 15−25 Ω/sq, Sigma−Aldrich). Substrates are cleaned by sonication for 20 min in each of the following solutions: 2% Hellmanex II detergent, deionized water, and isopropanol. Substrates are then immediately dried in a clean nitrogen stream. PEDOT:PSS films 25 ± 5 nm thick are spun-cast in air on top of the ITO anode, then baked for 10 min at 140 °C. Substrates are transferred to a nitrogen-purged glovebox, and the ITO/PEDOT:PSS stack is coated with a P3HT film 60 ± 5 nm thick. In some cases, the P3HT film is prebaked at 150 °C for 2 min (to remove residual solvent). The active layer is built following the scheme in Figure 1. First, samples are transferred to the EBL instrument for cross-linking. Second, samples are transferred back to the nitrogen-purged glovebox for image development. Third, PCBM films 32 ± 5 nm thick are spun-cast on top of the patterned P3HT films from 0.005 g/mL suspensions in DCM. Fourth, samples are transferred to a thermal evaporator for deposition of a 100-nm-thick Al cathode. Last, samples are returned to the glovebox to thermally anneal the active layer at 170 °C for up to 6 min. Note that samples are transferred between instruments using a portable chamber that is pressurized with nitrogen.

**Nanostructured Heterojunctions.** Nanostructured heterojunctions are built with the scheme illustrated in Figure 1, which is similar to the procedures for gradient heterojunctions. The key steps that differ for nanostructured devices are as follows. Prior to EBL, the P3HT films are baked at 150 °C for 2 min. P3HT nanostructures are developed with *p*-xylene at 35 °C for 25 s; the developer is purged with nitrogen to displace dissolved oxygen. The PCBM spin-casting step is performed twice using a 0.015 g/mL suspension of PCBM in DCM. We found that a "double-coat" process was more effective at filling the void space around the pillars (see Figure 6). The PCBM layer on top of nanostructures was 20−40 nm thick. After measuring the electronic function, the Al cathode is dissolved with aqueous potassium hydroxide (KOH, 45 wt %) and then PCBM is washed out with DCM. Device "deconstruction" is very valuable for confirming the P3HT nanostructures are intact after all processing steps.

**Bulk Heterojunctions.** BHJs are prepared with the same anode and cathode as gradient or nanostructured devices. The only step that differs is casting of the active layer. P3HT and PCBM are dissolved in a 1:1 ratio (weight basis) in anhydrous chlorobenzene (concentration of 0.01 g/mL). The solution is filtered three times, using a 0.2 μm Teflon mesh, and then a 100-nm-thick film is spun-cast on top of the PEDOT:PSS/ITO anode.

**Sequential Casting Heterojunctions.** These devices are prepared with the same anode and cathode as all other devices. The only step that differs is casting of the active layer. P3HT films are spun-cast on the PEDOT:PSS film with a thickness of 60 ± 5 nm, and the PCBM is spun-cast on top with a thickness of 32 ± 5 nm. The concentration of PCBM in DCM is 0.005 g/mL.

**Etching.** We used oxygen plasma to etch through the active layer so we could evaluate the internal structure. The oxygen plasma was generated with a Oxford Plasma Lab 80 Plus Reactive Ion Etch system (100 W, 20 sccm, 20 mTorr, DC bias of 230 V). The etch rates for P3HT and PCBM are ~0.75 and 0.5 nm/s, respectively, so the P3HT pillars appear shorter than the surrounding PCBM.

**Electronic Characterization.** All electronic measurements are conducted in a nitrogen-purged glovebox at 28 °C. Devices are illuminated with a 150 W solar simulator (Oriel) equipped with an air mass 1.5 global filter. The lamp power is calibrated to 100 mW/cm$^2$, using a silicon reference solar cell equipped with KG5 filter (certified by the National Renewable Energy Laboratory (NREL), VLSI Standards).[70] Current−voltage characteristics are recorded with a Keithley Model 2601A source meter. Power-conversion efficiency (PCE) is calculated from the open-circuit voltage ($V_{oc}$), short-circuit current density ($J_{sc}$), fill factor (FF), and input power ($P$) in the usual way:[70]

$$\mathrm{PCE} = \frac{V_{oc} J_{sc} \mathrm{FF}}{P} \quad (1)$$

To convert from current to current density, the device active area is calculated from the cathode area (measured from analysis of optical micrographs). Typical active areas are 0.03−0.05 cm$^2$.

## ■ ASSOCIATED CONTENT

### Supporting Information

(i) Measurements of irradiated PEDOT:PSS films (UV−vis, IR, and lithographic sensitivity); (ii) GIWAXS and UV−vis data for irradiated P3HT films; (iii) Proposed cross-linking mechanism for P3HT; (iv) Additional AFM measurements of P3HT nanostructures and P3HT/PCBM heterojunctions that demonstrate solvent-resistance and thermal stability; (v) AFM measurements of P3HT nanostructures that support the

concept of trapped radicals. This information is available free of charge via the Internet at http://pubs.acs.org/.

## ■ AUTHOR INFORMATION


### Corresponding Author

*E-mail: gestein@uh.edu.

### Author Contributions

[§]Equally contributing authors.


### Notes

The authors declare no competing financial interest.

## ■ ACKNOWLEDGMENTS

The authors acknowledge financial support by the Texas Center for Superconductivity, the National Science Foundation CAREER Award under Grant No. DMR 1151468, and the Department of Chemical and Biomolecular Engineering at the University of Houston. Use of the Advanced Photon Source was supported by the U.S. Department of Energy, Office of Science, Office of Basic Energy Sciences, under Contract No. DE-AC02-06CH11357. We thank Joseph Strzalka for assistance with GIWAXS measurements and Peter Vekilov for use of the MultiMode AFM. We appreciate assistance from the staff at the University of Houston Nanofabrication Facility.

## ■ REFERENCES


(1) Thompson, B.; Frechet, J. *Angew. Chem., Int. Ed.* **2008**, *47*, 58−77.
(2) Deibel, C.; Dyakonov, V. *Rep. Prog. Phys.* **2010**, 73.
(3) Brady, M. A.; Su, G. M.; Chabinyc, M. L. *Soft Matter* **2011**, *7*, 11065−11077.
(4) Woo, C.; Thompson, B.; Kim, B.; Toney, M.; Frechet, J. *J. Am. Chem. Soc.* **2008**, *130*, 16324−16329.
(5) Hammond, M. R.; Kline, R. J.; Herzing, A. A.; Richter, L. J.; Germack, D. S.; Ro, H.-W.; Soles, C. L.; Fischer, D. A.; Xu, T.; Yu, L.; Toney, M. F.; DeLongchamp, D. M. *ACS Nano* **2011**, *5*, 8248−8257.
(6) Weickert, J.; Dunbar, R.; Hesse, H.; Wiedemann, W.; Schmidt-Mende, L. *Adv. Mater.* **2011**, *23*, 1810−1828.
(7) Segalman, R. A.; McCulloch, B.; Kirmayer, S.; Urban, J. J. *Macromolecules* **2009**, *42*, 9205−9216.
(8) Botiz, I.; Darling, S. B. *Mater. Today* **2010**, *13*, 42−51.
(9) Botiz, I.; Schaller, R. D.; Verduzco, R.; Darling, S. B. *J. Phys. Chem. C* **2011**, *115*, 9260−9266.
(10) Xin, H.; Ren, G.; Kim, F.; Jenekhe, S. *Chem. Mater.* **2008**, *20*, 6199−6207.
(11) Xin, H.; Reid, O.; Ren, G.; Kim, F.; Ginger, D.; Jenekhe, S. *ACS Nano* **2010**, *4*, 1861−1872.
(12) Kim, J.; Park, Y.; Lee, D.; Lee, J.; Park, J.; Kim, J.; Cho, K. *Adv. Funct. Mater.* **2010**, *20*, 540−545.
(13) Kim, M.-S.; Kim, J.-S.; Cho, J.; Shtein, M.; Guo, L.; Kim, J. *Appl. Phys. Lett.* **2007**, 90.
(14) Aryal, M.; Buyukserin, F.; Mielczarek, K.; Zhao, X.-M.; Gao, J.; Zakhidov, A.; Hu, W. *J. Vac. Sci. Technol., B* **2008**, *26*, 2562−2566.
(15) Aryal, M.; Trivedi, K.; Hu, W. *ACS Nano* **2009**, *3*, 3085−3090.
(16) Haberkorn, N.; Gutmann, J.; Theato, P. *ACS Nano* **2009**, *3*, 1415−1422.
(17) Shih, C.; Hung, K.; Wu, J.; Hsiao, C.; Li, W. *Appl. Phys. Lett.* **2009**, 94.
(18) Wiedemann, W.; Sims, L.; Abdellah, A.; Exner, A.; Meier, R.; Musselman, K.; MacManus-Driscoll, J.; Mueller-Buschbaum, P.; Scarpa, G.; Lugli, P.; Schmidt-Mende, L. *Appl. Phys. Lett.* **2010**, 96.
(19) He, X.; Gao, F.; Tu, G.; Hasko, D.; Huettner, S.; Steiner, U.; Greenham, N.; Friend, R.; Huck, W. *Nano Lett.* **2010**, *10*, 1302−1307.
(20) He, X.; Gao, F.; Tu, G.; Hasko, D.; Huettner, S.; Greenham, N.; Steiner, U.; Friend, R.; Huck, W. T. *Adv. Funct. Mater.* **2011**, *21*, 139−146.
(21) Olsen, B.; Segalman, R. *Mater. Sci. Eng., R.* **2008**, *62*, 37−66.
(22) Coakley, K.; Srinivasan, B.; Ziebarth, J.; Goh, C.; Liu, Y.; McGehee, M. *Adv. Funct. Mater.* **2005**, *15*, 1927−1932.
(23) Chen, D.; Zhao, W.; Russell, T. P. *ACS Nano* **2012**, *6*, 1479−1485.
(24) Cai, S.; Keana, J.; Nabity, J.; Wybourne, M. *J. Mol. Electron.* **1991**, *7*, 63−68.
(25) Persson, S.; Dyreklev, P.; Inganas, O. *Adv. Mater.* **1996**, *8*, 405−408.
(26) Hikmet, R.; Thomassen, R. *Adv. Mater.* **2003**, *15*, 115−119.
(27) Nabity, J.; Wybourne, M. *Rev. Sci. Instrum.* **1989**, *60*, 27−32.
(28) Ocola, L. E.; Stein, A. *J. Vac. Sci. Technol., B* **2006**, *24*, 3061−3065.
(29) Ocola, L. E.; Tirumala, V. R. *J. Vac. Sci. Technol., B* **2008**, *26*, 2632−2635.
(30) Hu, W.; Sarveswaran, K.; Lieberman, M.; Bernstein, G. *J. Vac. Sci. Technol., B* **2004**, *22*, 1711−1716.
(31) Abdou, M.; Diazguijada, G.; Arroyo, M.; Holdcroft, S. *Chem. Mater.* **1991**, *3*, 1003−1006.
(32) Abdou, M.; Zi, W.; Leung, A.; Holdcroft, S. *Synth. Met.* **1992**, *52*, 159−170.
(33) Manceau, M.; Rivaton, A.; Gardette, J.-L.; Guillerez, S.; Lemaitre, N. *Polym. Degrad. Stab.* **2009**, *94*, 898−907.
(34) Gearba, I. R.; Nam, C.-Y.; Pindak, R.; Black, C. T. *Appl. Phys. Lett.* **2009**, 95.
(35) Sundberg, M.; Inganas, O.; Stafstrom, S.; Gustafsson, G.; Sjogren, B. *Solid State Commun.* **1989**, *71*, 435−439.
(36) Brown, P.; Thomas, D.; Kohler, A.; Wilson, J.; Kim, J.; Ramsdale, C.; Sirringhaus, H.; Friend, R. *Phys. Rev. B* **2003**, 67.
(37) Abdou, M.; Holdcroft, S. *Macromolecules* **1993**, *26*, 2954−2962.
(38) Zhao, J.; Swinnen, A.; Van Assche, G.; Manca, J.; Vanderzande, D.; Van Mele, B. *J. Phys. Chem. B* **2009**, *113*, 1587−1591.
(39) Kim, Y.; Choulis, S. A.; Nelson, J.; Bradley, D. D. C.; Cook, S.; Durrant, J. R. *Appl. Phys. Lett.* **2005**, 86.
(40) Hopkinson, P.; Staniec, P.; Pearson, A.; Dunbar, A.; Wang, T.; Ryan, A.; Jones, R.; Lidzey, D.; Donald, A. *Macromolecules* **2011**, *44*, 2908−2917.
(41) van der Gon, A.; Birgerson, J.; Fahlman, M.; Salaneck, W. *Org. Electron.* **2002**, *3*, 111−118.
(42) Ayzner, A.; Tassone, C.; Tolbert, S.; Schwartz, B. *J. Phys. Chem. C* **2009**, *113*, 20050−20060.
(43) Lee, K. H.; Schwenn, P. E.; Smith, A. R. G.; Cavaye, H.; Shaw, P. E.; James, M.; Krueger, K. B.; Gentle, I. R.; Meredith, P.; Burn, P. L. *Adv. Mater.* **2011**, *23*, 766−769.
(44) Gevaerts, V. S.; Koster, L. J. A.; Wienk, M. M.; Janssen, R. A. J. *ACS Appl. Mater. Interfaces* **2011**, *3*, 3252−3255.
(45) Chen, D.; Liu, F.; Wang, C.; Nakahara, A.; Russell, T. *Nano Lett.* **2011**, *11*, 2071−2078.
(46) Chen, D.; Nakahara, A.; Wei, D.; Nordlund, D.; Russell, T. *Nano Lett.* **2011**, *11*, 561−567.
(47) Treat, N.; Brady, M.; Smith, G.; Toney, M.; Kramer, E.; Hawker, C.; Chabinyc, M. *Adv. Energy Mater.* **2011**, *1*, 82−89.
(48) Kozub, D. R.; Vakhshouri, K.; Orme, L. M.; Wang, C.; Hexemer, A.; Gomez, E. D. *Macromolecules* **2011**, *44*, 5722−5726.
(49) Cravino, A.; Schilinsky, P.; Brabec, C. J. *Adv. Funct. Mater.* **2007**, *17*, 3906−3910.
(50) Gupta, D.; Bag, M.; Narayan, K. S. *Appl. Phys. Lett.* **2008**, 93.
(51) Brabec, C.; Shaheen, S.; Winder, C.; Sariciftci, N.; Denk, P. *Appl. Phys. Lett.* **2002**, *80*, 1288−1290.
(52) Ahlswede, E.; Hanisch, J.; Powalla, M. *Appl. Phys. Lett.* **2007**, 90.
(53) Kim, B.; Miyamoto, Y.; Ma, B.; Frechet, J. *Adv. Funct. Mater.* **2009**, *19*, 2273−2281.
(54) Shaw, P.; Ruseckas, A.; Samuel, I. *Adv. Mater.* **2008**, *20*, 3516−3519.
(55) Muller, C.; Falcou, A.; Reckefuss, N.; Rojahn, M.; Wiederhirn, V.; Rudati, P.; Frohne, H.; Nuyken, O.; Becker, H.; Meerholz, K. *Nature* **2003**, *421*, 829−833.
(56) Krebs, F. *Sol. Energy Mater. Sol. Cells* **2009**, *93*, 394−412.
(57) Miyanishi, S.; Tajima, K.; Hashimoto, K. *Macromolecules* **2009**, *42*, 1610−1618.

(58) Kim, H.; Han, A.-R.; Cho, C.-H.; Kang, H.; Cho, H.-H.; Lee, M.; Frechet, J.; Oh, J.; Kim, B. *Chem. Mater.* **2011**, *24*, 215−221.
(59) Jegadesan, S.; Taranekar, P.; Sindhu, S.; Advincula, R.; Valiyaveettil, S. *Langmuir* **2006**, *22*, 3807−3811.
(60) Jegadesan, S.; Sindhu, S.; Advincula, R.; Valiyaveettil, S. *Langmuir* **2006**, *22*, 780−786.
(61) Jiang, G.; Baba, A.; Advincula, R. *Langmuir* **2007**, *23*, 817−825.
(62) Park, J. Y.; Taranekar, P.; Advincula, R. *Soft Matter* **2011**, *7*, 1849−1855.
(63) O'Brien, G.; Quinn, A.; Tanner, D.; Redmond, G. *Adv. Mater.* **2006**, *18*, 2379−2382.
(64) Sokolov, A.; Roberts, M.; Bao, Z. *Mater. Today* **2009**, *12*, 12−20.
(65) Ruchhoeft, P.; Wolfe, J. *J. Vac. Sci. Technol., B* **2001**, *19*, 2529−2532.
(66) Parekh, V.; Chunsheng, E.; Smith, D.; Ruiz, A.; Wolfe, J.; Ruchhoeft, P.; Svedberg, E.; Khizroev, S.; Litvinov, D. *Nanotechnology* **2006**, *17*, 2079−2082.
(67) Parekh, V.; Ruiz, A.; Ruchhoeft, P.; Nounu, H.; Litvinov, D.; Wolfe, J. *J. Vac. Sci. Technol., B* **2006**, *24*, 2915−2919.
(68) Nasrullah, A.; Smith, D.; Sherlock, T.; Ruchhoeft, P.; Litvinov, D. *J. Vac. Sci. Technol., B* **2009**, *27*, 2674−2678.
(69) Perera, G. M.; Stein, G. E.; Liddle, J. A. *J. Vac. Sci. Technol., B* **2010**, *28*, 1048−1055.
(70) Shrotriya, V.; Li, G.; Yao, Y.; Moriarty, T.; Emery, K.; Yang, Y. *Adv. Funct. Mater.* **2006**, *16*, 2016−2023.